

# Does supernova feedback regulate the star formation rate in dwarf galaxies?

D. J. Whitworth,<sup>1,2\*</sup> E. Vázquez-Semadeni,<sup>1</sup> J. Ballesteros-Paredes,<sup>1</sup> G. C. Gómez,<sup>1</sup>

<sup>1</sup>Universidad Nacional Autónoma de México. Instituto de Radioastronomía y Astrofísica. Apdo. Postal 72-3 (Xangari), Morelia, Michoacán 58089, México

<sup>2</sup>Centre de Recherche Astrophysique de Lyon UMR5574, ENS de Lyon, Univ. Lyon1, CNRS, Université de Lyon, 69007, Lyon, France

Accepted XXX. Received YYY; in original form ZZZ

## ABSTRACT

Stars form in cold, dense clouds embedded in galactic discs, but whether their formation is primarily regulated by gravitational collapse, turbulence, or stellar feedback remains unclear. Using four high-resolution dwarf galaxy simulations with and without supernova (SN) feedback and magnetic fields, we test how feedback regulates the supply of dense gas and, consequently, the star formation rate (SFR). Although the SFR does increase when SNe are turned off, this increase is only by a factor of a few. Instead, across all models, the theoretical maximum SFR originally proposed by Zuckerman and Palmer, defined as the ratio of the total dense gas mass to its mean free-fall time ( $M_{\text{dense}}/\tau_{\text{ff}}$ ), always exceeds the measured SFR by nearly two orders of magnitude. Moreover, the increase of the SFR in the case without SNe is accompanied by a nearly corresponding increase of the total dense gas mass ( $M_{\text{dense}}$ ), such that the dense-gas depletion time,  $\tau \equiv \text{SFR}/M_{\text{dense}}$ , decreases by only  $\sim 33\%$  in the hydrodynamical case and by about 55% in the magnetohydrodynamical models. This indicates that SN feedback does not primarily act by slowing the collapse of dense gas, but instead by limiting how much diffuse gas can be converted into dense gas. Our results suggest that the main contribution to the regulation of the SFR, at least in dwarf galaxies, may arise from stabilization by galactic rotation, rather than by SN feedback.

**Key words:** keyword1 – keyword2 – keyword3

## 1 INTRODUCTION

One of the fundamental problems concerning star formation (SF) in galaxies was posed decades ago by Zuckerman & Palmer (1974), who pointed out that, if all molecular clouds in the Milky Way were undergoing free-fall collapse, the resulting Galactic star formation rate (SFR) would be much larger than the observed value. They estimated this theoretical maximum SFR (hereafter labelled  $\text{SFR}_{\text{max}}$ ) as

$$\text{SFR}_{\text{max}} \approx \frac{M_{\text{mol}}}{\tau_{\text{ff}}(\bar{\rho})}, \quad (1)$$

where  $M_{\text{mol}}$  is the total mass in molecular gas in the Galaxy, and

$$\tau_{\text{ff}}(\bar{\rho}) \equiv \left( \frac{3\pi}{32G\bar{\rho}} \right)^{1/2} \quad (2)$$

is the free-fall time for the mean density  $\bar{\rho}$  of the molecular gas. For a total molecular gas mass  $M_{\text{mol}} \approx 10^9 M_{\odot}$  (Heyer & Dame 2015) and a mean number density  $n \approx 100 \text{ cm}^{-3}$ , one finds  $\text{SFR}_{\text{max}} \sim 300 M_{\odot} \text{ yr}^{-1}$ , roughly two orders of magnitude larger than current observational estimates of the SFR of  $\sim 2 M_{\odot} \text{ yr}^{-1}$  (Chomiuk & Povich 2011).

Such a large discrepancy between the theoretical maximum SFR and the observed value, to which we refer as *the star formation conundrum*, has been in general attributed to the effect of stellar feedback on clouds, either by driving turbulence that prevents their collapse and maintains them in approximate virial equilibrium or causes them to be gravitationally unbound (e.g., Zuckerman & Evans 1974; Mac Low & Klessen 2004; McKee & Ostriker 2007; Padoan et al. 2016; Evans et al. 2021; Grudić et al. 2022; Kim et al. 2022; Ballesteros-Paredes et al. 2024; Krumholz et al. 2025), or by destroying collapsing molecular clouds long before most of their mass has been converted into stars (e.g., Field 1970; Franco et al. 1994; Colín et al. 2013; Mac Low et al. 2017; Vázquez-Semadeni et al. 2019).

However, the precise mechanism by which stellar feedback can reduce the SFR is not fully understood. Supernova (SN) feedback on molecular clouds is often considered the main energy-injection mechanism to interstellar turbulence from massive stars (e.g., Mac Low & Klessen 2004; Padoan et al. 2016), and indeed, it has been found to significantly reduce the SFR in comparison to simulations not including it (Khullar et al. 2024). However, how this compares to the  $\text{SFR}_{\text{max}}$  estimate was not considered by those authors. Moreover, the effect of SN feedback on clouds appears to depend

\* E-mail: david.whitworth@ens-lyon.fr

strongly on the distance between the SN and the cloud (Iffrig & Hennebelle 2015), and the net driving efficiency of ISM turbulence by SNe appears to be rather low, between 1.5 and 4.5% (Iffrig & Hennebelle 2017). Furthermore, Brucy et al. (2020, 2023) have suggested, through kiloparsec-scale numerical simulations, that in high-surface density galaxies, stellar feedback is insufficient to reduce the SFR to realistic levels, and that additional sources of turbulence, forms of support, or effects may be necessary in these cases.

In addition, pre-SN photoionizing radiation from massive stars is also an important agent in regulating the SFR, since they act *inside* the clouds, in contrast to the effect of SNe, which typically explode *outside* the clouds (Geen et al. 2016; Vázquez-Semadeni et al. 2019; Chevance et al. 2022; Bending et al. 2022). Thus, while SN explosions can contribute to either cloud formation by external compression (e.g., Inutsuka et al. 2015) or to cloud erosion by stirring their outskirts (Iffrig & Hennebelle 2015), photoionizing feedback works exclusively to destroy the clouds (e.g., Matzner 2002; Haid et al. 2019). In conclusion, the precise effect of stellar feedback is not well constrained yet.

Magnetic support is one of the most frequently invoked mechanisms (other than feedback) to reduce the SFR (e.g., Hennebelle & Inutsuka 2019; Krumholz & Federrath 2019), but, on the other hand, Zamora-Avilés et al. (2018) have shown that moderate-intensity fields can actually *speed up* star formation by inhibiting turbulence generation during cloud assembly, and thus allowing faster onset of collapse. Additionally, Whitworth et al. (2023) have recently found that magnetic fields do not seem to reduce the global SFR in low-metallicity dwarf galaxies. Therefore, the precise effect of magnetic fields in the regulation of the *global* SFR also remains unclear.

Of course, a crucial form of support for the gas on scales larger than a few hundred parsecs in spiral galaxies is the rotation itself, although it is well known that it has to be complemented by significant on-plane velocity fluctuations in order to be fully stabilized (e.g., Safronov 1960; Toomre 1964; Rafikov 2001). In this paper we contribute to the understanding of the role of various mechanisms by comparing the relative contribution of rotation, feedback-induced turbulence, and magnetic fields to the regulation of the SFR in the disks of dwarf galaxies, using numerical simulations where the different processes are alternatively turned on and off. The plan of the paper is as follows: Section 2 discusses the set up of the simulations used in this study. Section 3 presents the results of our analysis. Section 4 analyses our results in the context of the dense gas reservoirs and star formation and in Section 5 we summarise our key findings.

## 2 METHODS

### 2.1 Numerical Modelling

For this work we use the quasi-Lagrangian moving mesh code AREPO (Springel 2010). It solves the ideal magnetohydrodynamic (MHD) equations on a 3D unstructured Voronoi mesh. This allows the Voronoi cells to trace the local gas velocity (Pakmor et al. 2011). After each time step,  $\sim 1$  Myr, the cells are restructured. By doing this, the code allows for a continuous and adaptive resolution whilst keeping the mass in

the cells relatively constant, only varying by up to a factor of two. We use a Jeans (1902) length criterion to ensure this length is always resolved with at least 8 cells (Truelove et al. 1997; Federrath et al. 2011). This ensures we avoid artificial fragmentation and makes sure the collapsing gas is fully resolved. We employ the Powell et al. (1999) divergence cleaning method along with an HLLD Riemann solver (Miyoshi & Kusano 2005) in order to mitigate the divergence errors that arise in MHD models. For a more detailed discussion on AREPO we point to Springel (2010), Pakmor et al. (2011), and Whitworth et al. (2023), which described the specific models used in this work in more detail. However, below we present a brief discussion on the setup used.

The ISM model implemented here is the same as in Whitworth et al. (2022) and Whitworth et al. (2023, hereafter Paper I). It uses a non-equilibrium, time-dependent, chemical network based on the work of Gong et al. (2017), which includes cosmic-ray ionization. The self-shielding of dissociating ultraviolet (UV) radiation is modelled using the TreeCol algorithm of Clark et al. (2012) with a shielding radius of 30 pc. We take the molecular and atomic cooling functions from Clark et al. (2019), which were originally described by Glover et al. (2010). We are able to directly trace nine non-equilibrium species ( $\text{H}_2$ ,  $\text{H}^+$ ,  $\text{C}^+$ ,  $\text{CH}_x$ ,  $\text{OH}_x$ ,  $\text{CO}$ ,  $\text{HCO}^+$ ,  $\text{He}^+$  and  $\text{Si}^+$ ) and through conservation laws derive a further eight (free electrons,  $\text{H}$ ,  $\text{H}_3^+$ ,  $\text{C}$ ,  $\text{O}$ ,  $\text{O}^+$ ,  $\text{He}$  and  $\text{Si}$ ).

We model star formation with an accreting sink particle model where each sink represents a star forming region of gas. To make sure the gas that forms the sink is collapsing and truly self gravitating and the sink can be considered star forming, a sink is only formed if gas above a density threshold of  $\rho_c$ , of  $2.4 \times 10^{-21} \text{ g cm}^{-3}$  (equivalent to  $n = 10^3 \text{ cm}^{-3}$ ) and within an accretion radius,  $r_{\text{acc}}$ , of 1.75 pc satisfies the following criteria:

- (i) The gas flow must be converging with negative divergence of both velocity and acceleration.
- (ii) The region must be centred on a local potential minimum.
- (iii) The region must not fall within the accretion radius of another sink particle.
- (iv) The region should not move within the accretion radius of other sink particles in a time less than the local free-fall time.
- (v) The region must be gravitationally bound.

If all criteria are met, then the cell(s) form a sink particle of mass up to  $200 M_\odot$  with the accreted mass from a cell limited to 90% of the cells mass.

After a sink has formed it will continue to accrete gas from the surrounding cells only if the cell is within  $r_{\text{acc}}$ , above  $\rho_c$  and gravitationally bound, i.e. the gas is in falling due to gravitational acceleration above the threshold density within the accretion radius, to the sink. We discretise the mass in the sink to determine a stellar populations based on the method presented in Sormani et al. (2017) with an assumed star formation efficiency in the sink of  $\epsilon_{\text{SF}} = 0.1$ . The remainder of the mass is considered to be gas. We do this as even though the models presented here are high resolution it is still not high enough to model individual stars and at the sink creation density star formation is inefficient (Krumholz & McKee 2005; Evans et al. 2009).

If we have stars of mass greater than  $8 M_\odot$ , once they

reach the end of their life they generate a supernova explosion (SNe). The SNe injection routines are described in detail in Whitworth et al. (2022) and Tress et al. (2020). The energy from a SN is injected over a radius  $R_{\text{inj}}$ , which is set to 16 cells. If  $R_{\text{inj}}$  is greater than the radius of the remnant at the end of its Sedov-Taylor phase ( $R_{\text{ST}}$ ), i.e. if  $R_{\text{ST}} < R_{\text{inj}}$ , we inject energy into the ISM by setting the temperature in the bubble to  $10^4$  K, and let the ionisation state of the gas to evolve from the injected temperature. If, however,  $R_{\text{ST}} > R_{\text{inj}}$ , then we directly inject  $10^{51}$  erg into the gas as thermal energy and fully ionise the gas. We only include type IIa supernova and therefore are likely to slightly under predict the rates compared to the expected rates in Magellanic clouds of 2.5-4.6 SNe per millennium (Maoz & Badenes 2010) and an expected one type Ia SNe for every 4-6 type IIa core collapse SNe.

We also inject mass evenly distributed into the surrounding gas at the scale of the energy injection via  $M_{\text{in}} = (M_{\text{sink}} - M_{\text{stars}})/n\text{SN}$ , where  $M_{\text{in}}$  is the injected mass,  $M_{\text{sink}}$  is the mass of the sink at the time of the SNe,  $M_{\text{stars}}$  is the mass of stars in the sink and  $n\text{SN}$  is the number of remaining SNe that the sink will produce. After the last SNe has occurred, the sink is considered to be fully-stellar mass and is converted into a collisionless  $N$ -body star particle. If a sink is unable to produce SNe due to being populated with low mass stars, then after 10 Myr, a fraction,  $\epsilon_{\text{SF}} = 0.1$ , of its mass is turned into a star particle with the rest being returned as gas to the surrounding cells.

For a more detailed description of the code and our custom physics modules, see Paper I and Whitworth et al. (2022).

## 2.2 Initial Conditions

For the models presented in this work we take our initial conditions as the 930 Myr snapshot from model MHD\_SAT presented in Whitworth et al. (2023). Here we describe the set up for that model and in the following section the changes made for the 3 new simulations completed for this work.

The initial, isolated, low metallicity dwarf galaxy is modelled as a disc consisting of two components: a dark matter halo and a gaseous disc. Sink particles are formed over time with no initial sink or star particle distribution implemented. By 930 Myr the sinks that are present have formed from the gaseous disc with a stellar background population having arisen from the sink particles over time.

The dark matter halo is modelled with a spheroidal Hernquist (1990) density profile:

$$\rho_{\text{sph}}(r) = \frac{M_{\text{sph}}}{2\pi} \frac{a}{r(r+a)^3}, \quad (3)$$

where  $r$  is the spherical radius,  $a = 7.62$  kpc is the scale-length of the halo, and  $M_{\text{sph}} = 2 \times 10^{10} M_{\odot}$  is the halo mass. The gaseous disc component is initially modelled as a double exponential density profile:

$$\rho_{\text{disc}}(R, z) = \frac{M_{\text{disc}}}{2\pi h_z h_R^2} \text{sech}^2\left(\frac{z}{2h_z}\right) \exp\left(-\frac{R}{h_R}\right), \quad (4)$$

where  $R$  is the cylindrical radius and  $z$  is height above the mid-plane,  $M_{\text{disc}} = 8 \times 10^7 M_{\odot}$  is the gas mass of the disc, and  $h_z = 0.35$  kpc and  $h_R = 0.82$  kpc are its scale-height and scale-length, respectively. See Table 1 for the initial component parameters.

	Mass ( $M_{\odot}$ )	Scale length (kpc)	$h_z$ (kpc)
DM Halo	$2.00 \times 10^{10}$	7.62	-
Gas disc	$8.00 \times 10^7$	0.82	0.35

**Table 1.** Parameters for the different galactic components

Model	Z ( $Z_{\odot}$ )	$\log_{10} \xi$	$\zeta_{\text{H}}$ ( $\text{s}^{-1}$ )	$G$ ( $G_{\odot}$ )	$\log_{10} B$ ( $\mu\text{G}$ )
MHD_SAT	0.10	-3	$3 \times 10^{-18}$	0.17	-2

**Table 2.** Values used in the initial conditions for MHD\_SAT for metallicity  $Z$ , dust-to-gas ratio  $\xi$ , relative to the value in solar metallicity gas, cosmic ionisation rate  $\zeta_{\text{H}}$ , UV field strength  $G$ , and magnetic field strength  $B$ .

Model	SNe	$B$
Hydro	✓	×
Hydro no SNe	×	×
MHD	✓	✓
MHD no SNe	×	✓

**Table 3.** The four models used for this work showing which ones have the supernovae routine (SN) and magnetic field ( $B$ ) turned on

The seed magnetic field is initiated as a uniform, mono-directional, poloidal seed field of strength  $10^{-2} \mu\text{G}$ . At 930 Myr, the field has reached a steady state of mass-weighted  $|B| \sim 10 \mu\text{G}$  and volume-weighted  $|B| \sim 0.6 \mu\text{G}$ . The metallicity  $Z$ , dust-to-gas ratio  $\xi$  (which has a Solar neighbourhood value of  $\xi = 0.01$ ), cosmic ray ionisation rate of atomic hydrogen  $\zeta_{\text{H}}$ , far-ultraviolet (FUV) field strength  $G$  (given in Habing units  $G_{\odot}$ ) are all set to 10% of their solar neighbourhood values and listed in Table 2. These values are constant throughout the simulation. For a more detailed description of the initial setup we refer the reader to the original work, Paper I.

## 2.3 New models

We run three new models and continue run of MHD\_SAT for a further 75 Myr. The new models begin from the 930 Myr snapshot of MHD\_SAT as described above. This work aims to look at the importance of feedback and magnetic fields in the role of galactic star formation and how they affect the star formation rate (SFR). With respect to that the new models are designed to look into this. We take the snapshot at 930 Myr and modify it to represent different regimes. First, in model **MHD\_no\_SNe** we turn off the SNe routine but allow sinks to still form and accrete. For model **Hydro** we turn off the magnetic field but keep the SNe routine turned on. In Model **Hydro\_no\_SNe** we turn off both the SNe and the magnetic field. See Table 3.

We run models MHD and Hydro for 150 Myr from the snapshot at 930 Myr. This ensures that the Hydro model has reached a new steady state in star formation. When the magnetic field is turned off, pressure support in the ISM suddenly changes and decreases, creating a short burst in star formation. These new stars then generate more SNe, causing a short dynamical change in the disc. After a few Myr the SFR again reaches a steady state.

The models without SNe are run for as long as is com-

putationally possible. With no feedback in the models the gas has nothing to support it from undergoing self collapse due to gravity other than the rotation of the disc and magnetic field. This collapse into dense structures causes AREPO to hyper refine in the densest gas beyond the sink creation density and form millions of new cells. Whilst these cells only exist for a short time before being refined (see Section 2.4), this eventually becomes untenable in the code and it can no longer proceed. This happens after 50 Myr in Hydro\_no\_SNe model, and after 70 Myr in the MHD\_no\_SNe model, showing that the magnetic field does slow down the collapse of the gas into denser structures by roughly 40%.

## 2.4 Resolution

We keep the resolution the same as in the original work. The base target mass resolution for the gas cells is set to  $50 M_{\odot}$  using the default AREPO refinement scheme. The scheme keeps the cell mass within a factor of 2 of this target mass as cells merge and split during refinement. We also use a Jeans refinement criterion where by we resolve the Jeans Length by at least 8 cells. This implies that, at number densities of  $n = 100 \text{ cm}^{-3}$ , we reach an average cell radius ( $r_{\text{cell}}$ ) of 0.79 pc and, at  $n = 10^3 \text{ cm}^{-3}$ ,  $r_{\text{cell}}$  is 0.31 pc. Due to the fact that the cells range in both mass and size we adopt an adaptive softening for the gas cell size. In the initial conditions for the parent simulation we applied a fixed softening length to both the dark matter (64 pc) and the sink particles (2 pc).

One issue that arises with the scheme used in AREPO is that it allows for cells to go beyond the sink creation density depending on when the sinks form in the time-stepping process. Whilst these cells will typically only last for a single to a few small timesteps, they do exist, as can be seen in Figure 1. The sinks form at  $10^4 \text{ cm}^{-3}$ , the dashed line in the plot, and we see cells above that density. Once we remove the SNe there is little to disrupt the gravitational collapse of the dense gas and we end up with many more cells, up to a  $\sim 85\%$  increase, in the region which causes the code to become overloaded and cease. In our models this does not cause an issue, as we can see in various results that we have reached a new, if short, steady state period in star formation.

## 3 RESULTS

We present our results for each model in the following sections. We first look at the morphology of the gaseous disc and differences between them. We then present the magnetic field results and how they change when feedback is removed. Then, we focus on the SFR and compare it to the free-fall star formation rate, Equation (1), the theoretical maximum SFR for a dense gas cloud. Finally, we look into the stability of the gas in the form of the Toomre  $Q$  of both the total gas and the dense gas. All results, unless otherwise stated, are taken from the final snapshots of each model, Hydro and MHD at 1070 Myr, Hydro\_no\_SNe at 980 Myr and MHD\_no\_SNe at 998 Myr.

### 3.1 Morphology

We plot the HI surface density projections in Figure 2 for each model. The models with SNe, left hand plots, show a less filamentary structure, with more extended diffuse-gas regions across the projection compared to models without SNe, especially in the Hydro model. However, the MHD model does show some dense filamentary like structures, especially in the upper left quadrant. Whereas the Hydro model shows much fewer filamentary structures with less variation in the density when SNe are included. The models that exclude SNe feedback, the right hand plots, show more filamentary and spiral-like structures and voids. We also see that the MHD model has fewer large-scale voids compared to the Hydro model.

If we look at Figure 3 we can see that the voids are hot in the models with SNe, whilst when SNe are removed this hot gas obviously disappears. However, we can see that the cold gas in the Hydro model without SNe is much more sharply defined, whilst in the MHD the darker, colder regions are less well defined. So the magnetic field does not appear to be preventing thermal condensation but slowing the condensation of the gas into fine, dense, structures, supporting the idea that the field supports the gas against gravitational collapse.

Figure 4 shows the time averaged total gas and dense gas,  $n \geq 100 \text{ cm}^{-3}$ , azimuthally-averaged surface density radial profile for each model. There is little change in the total gas surface density with and without SNe, except for a very small increase in MHD and small decrease in Hydro when SNe are present. When SNe feedback is removed we see that the dense gas surface profile for both models increases, especially in the Hydro case, which increase by an order magnitude. In the MHD case it is similar in the central 0.5 kpc, but then stays higher to the point where it drops off at  $\sim 1.75$  kpc.

### 3.2 Magnetic Field

Figure 5 shows the magnetic field strength and field lines in both MHD models. The field is more organised in the model without SNe, exhibiting more stable spiral arm-like structures in the field. The field strength is also more evenly distributed across the disc with fewer low strength voids within it. This is expected as we are using ideal-MHD where the field traces the gas. As no SNe are creating large bulk motions in the gas, the field becomes more uniform since the gas distribution is less turbulent.

Figure 6 shows the temporal evolution of the volume-weighted mean field strength in the disc of each MHD simulation, where the disc is defined as the volume within  $r = 1.75$  kpc and  $z = \pm 0.3$  kpc over time. Both models increase in field strength at the start, but the model without SNe increases at a faster rate, from  $0.71 \mu\text{G}$  to  $0.93 \mu\text{G}$ , whilst the simulation with SNe only reaches  $0.80 \mu\text{G}$ . We cannot give a steady-state averaged volume-weighted field strength for the model without feedback, as it does not appear to be in a steady state in terms of field strength. However, the final snapshot has a volume-weighted field strength of  $0.90 \mu\text{G}$ . On the other hand, the model with SNe is in a steady state, having been simulated for a much longer time (Whitworth et al. 2023). For consistency with the star formation rate and other analysis in this work we take the steady state from 1 Gyr and report a volume-weighted average field strength of  $0.77 \mu\text{G}$ .

Figure 7 shows the  $B$ - $n$  relationship for each model. The

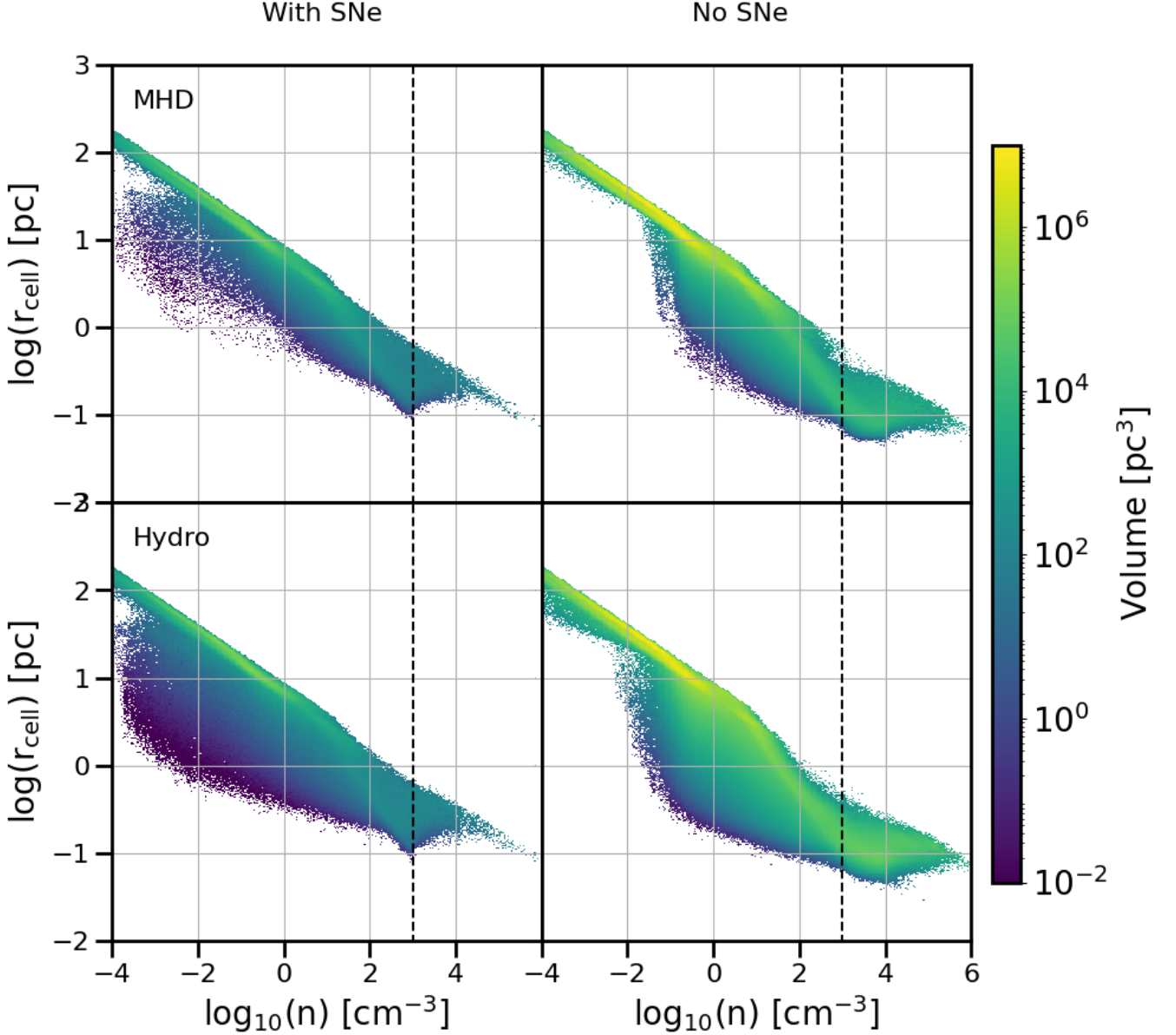


**Figure 1.** The mass weighted cell radius against number density for each of the simulations taken at the last snapshot. The dashed vertical line represents the sink creation density threshold. We can see here the increase in hyper refined cells in the models without supernova feedback.

black dotted line represents the volume-weighted average  $B$  for the simulations; the solid black line shows the result from Crutcher et al. (2010), whilst the red lines show the results from Whitworth et al. (2025). In the model with no feedback there are no SNe driving the hot, diffuse, turbulent gas, which is important in driving the growth of the small-scale dynamo (Gent et al. 2021; Whitworth et al. 2025). We see that the simulations do not follow the observational predictions, especially in the diffuse gas; this is discussed in more detail in Whitworth et al. (2025), where the importance of resolution is noted. The lack of very diffuse gas in the model without feedback is a result of a lack of SNe creating hot diffuse gas.

### 3.3 Star formation rates

To calculate the SFR we use the same method as in Whitworth et al. (2022). We calculate the mass accreted ( $M_{\text{acc}}$ ) onto sinks between snapshots as well as the mass in any new sink particles created ( $M_{\text{new}}$ ). We assume that not all the mass in the sink is star forming and apply an efficiency,  $\epsilon_{\text{SF}} = 0.1$ . We sum the masses and divide by the time between the current snapshot ( $t_2$ ) and the previous snapshot ( $t_1$ ),  $\delta t = t_2 - t_1$ :

$$\text{SFR} = \frac{(M_{\text{acc}} + M_{\text{new}})}{\delta t} \quad (5)$$

Whilst we include a star formation efficiency factor ( $\epsilon_{\text{SF}}$ ) in our calculation to represent the inefficiency of star formation

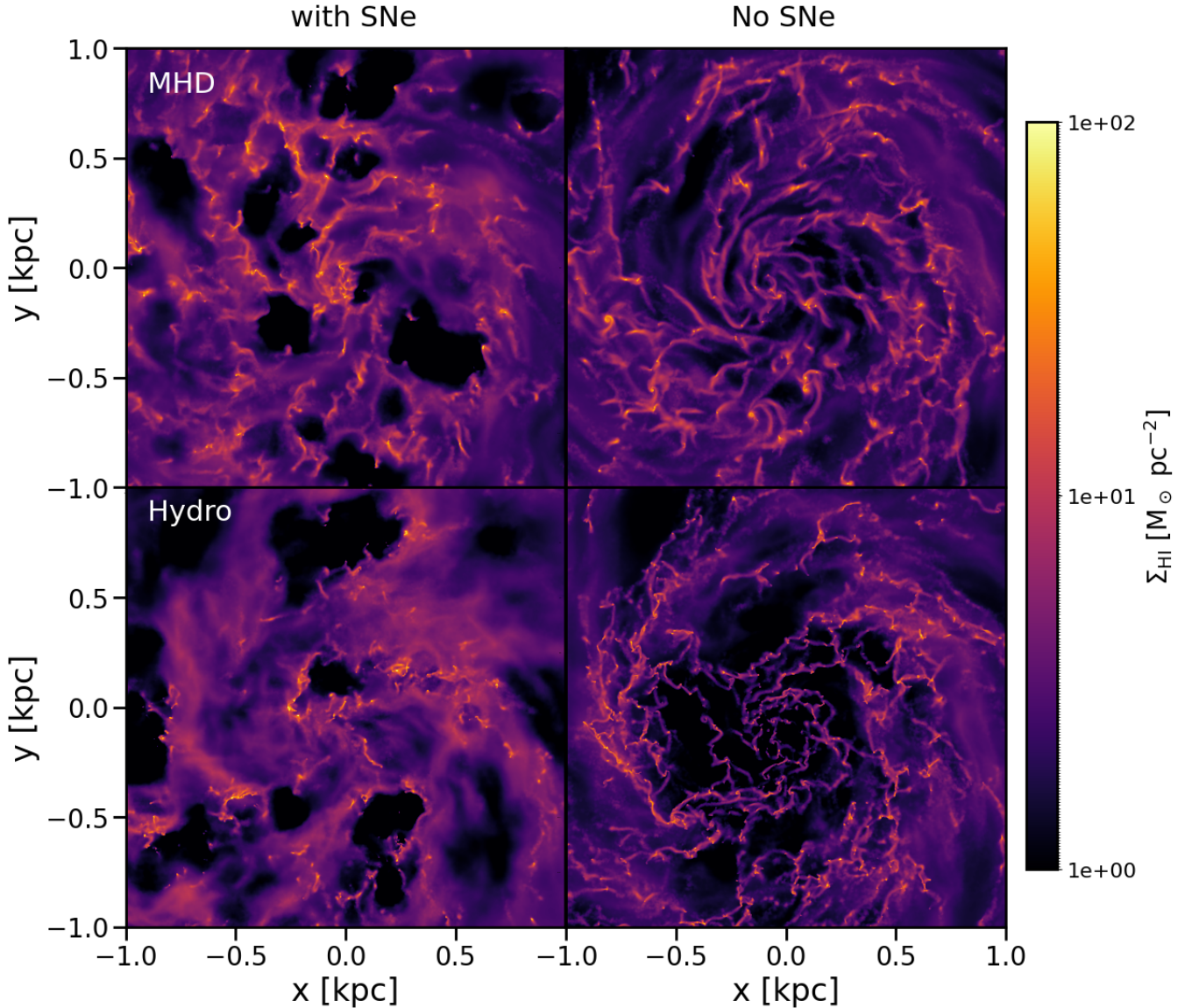


**Figure 2.** The HI gas surface density projections for each of the four models used in the analysis. The top row shows the hydrodynamical models, the bottom row shows the MHD models. On the left we show the models with SNe feedback, the right column has no SNe feedback. The dense filament structures that form due to self-gravity when there is no support from feedback in the gas can be clearly seen.

and that our sink particles represent core-like systems with multiple stellar objects in a gas cloud, we note we do not do this for  $\text{SFR}_{\text{max}}$ .  $\epsilon_{\text{SF}}$  is defined in our initial conditions. If we were to modify this to 1.0, we would assume that all the mass in the sink particle is in stars, thus changing the time when SNe occur and likely the number of supernovae a sink would produce; i.e., more mass means a possibility of more massive stars due to the random distribution drawn from the IMF.

Figure 8 shows the star formation rates (SFR) for each model (solid lines) as well as the upper limit,  $\text{SFR}_{\text{max}}$  (dotted lines). The black dashed and dashed-dotted vertical lines show the starting times of the periods we consider to be in a steady state, over which we calculate averages. These averaging periods end at the final time of each simulation. For the models without SNe this starting time is 955 Myr, and

for the models with SNe it is 1000 Myr. We take these times as from here the models have flat SFRs. We can see a burst in star formation when the magnetic field is turned off, occurring between 930 Myr and  $\sim 980$  Myr in the Hydro model (blue line). This also happens in the Hydro model with no feedback (cyan line), but we note that at  $\sim 950$  Myr the SFR appears to reach a steady state from  $\sim 950$  Myr. Finally, we also calculate the  $\text{SFR}_{\text{max}}$ , which is the theoretical maximum SFR based on the free-fall time of the gas calculated as in Equation (1) where  $M_{\text{mol}}$  is defined as the mass in dense gas above number densities of  $100 \text{ cm}^{-3}$ , and  $t_{\text{ff}}$  is the mean free-fall time of the dense gas.

Table 4 shows the average results of the steady state periods along with the ratio between  $\text{SFR}_{\text{max}}$  and the observed SFR, the total gas mass in dense gas ( $M_{\text{dense}}$ ) as well as the  $\text{SFR}_{\text{specific}}$  (the SFR per unit dense gas mass). We see

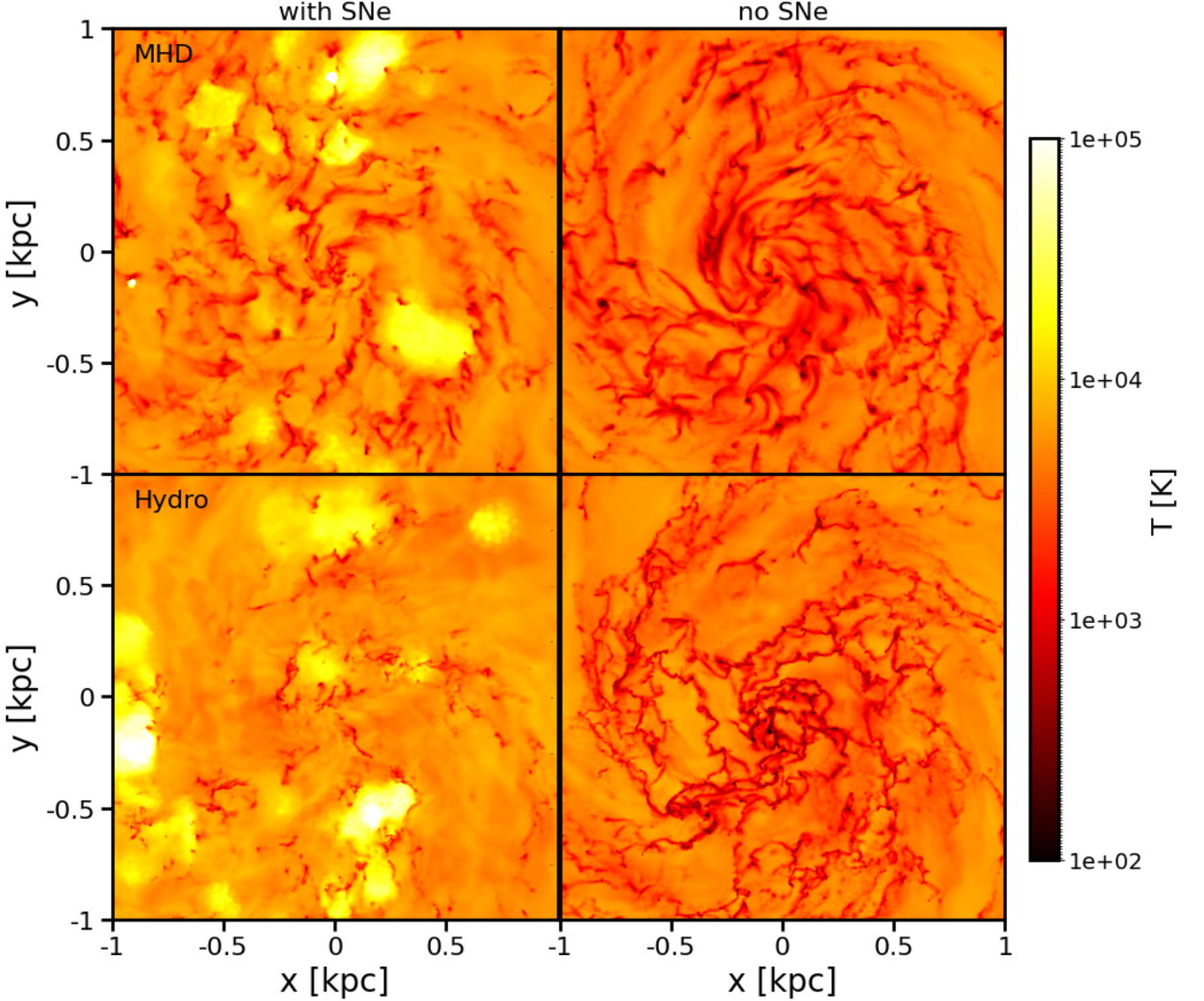


**Figure 3.** Integrated temperature projection of the 4 models. The diffuse voids seen in the SNe models in Figure 2 are seen as hot bright spots. Whereas the voids in the models without SNe are more consistent with the diffuse gas.

that the values for  $\text{SFR}_{\text{max}}$  are 1.7 to 1.8 orders of magnitude larger than the observed SFR in all simulations, ranging from a factor 51 in the Hydro simulation to 64 in Hydro\_no\_SNe.

We work out the star formation efficiency (SFE) for each simulation as:

$$\text{SFE} \equiv \frac{\text{SFR}}{\text{SFR}_{\text{max}}}, \quad (6)$$

and report the values in Table 4.

Figure 9 shows the depletion time ( $\tau$ ) of the total gas mass (column 2) in the disc and in the dense gas (column 3). We calculate it as:

$$\tau \equiv \frac{M_g}{\text{SFR}}, \quad (7)$$

where  $M_g$  is the mass in the gas. We also calculate the depletion time based on  $\text{SFR}_{\text{max}}$ , shown in column 4, and the ratio between the total gas depletion time and depletion time based on  $\text{SFR}_{\text{max}}$  in column 5. The depletion time ( $\tau$ ) from

$\text{SFR}_{\text{max}}$  is much shorter than for the actual measured SFR, and is shorter even than that for the dense gas with no SNe.

### 3.4 Stability

To understand our results, we investigate the stability of the gas in the ISM by looking at the Toomre Q parameter of both the total gas within the disc,  $r \leq 1.75$  kpc and  $|z| \leq 0.3$  kpc, and of the dense gas,  $n \geq 100\text{cm}^{-3}$  in the same volume. We calculate the Toomre parameter for the gas following Equation (27) from Rafikov (2001), in radial bins where the bin width is set by the largest cell size in each annulus, with a minimum of at least 100 pc, the expected scale of supernovae driving. As AREPO cells can vary significantly in shape and size, we allow a 5% overlap between bins to account for cells that may cross both annuli. We thus write:

$$Q_g = \frac{\kappa\sigma}{\pi G \Sigma_g}, \quad (8)$$

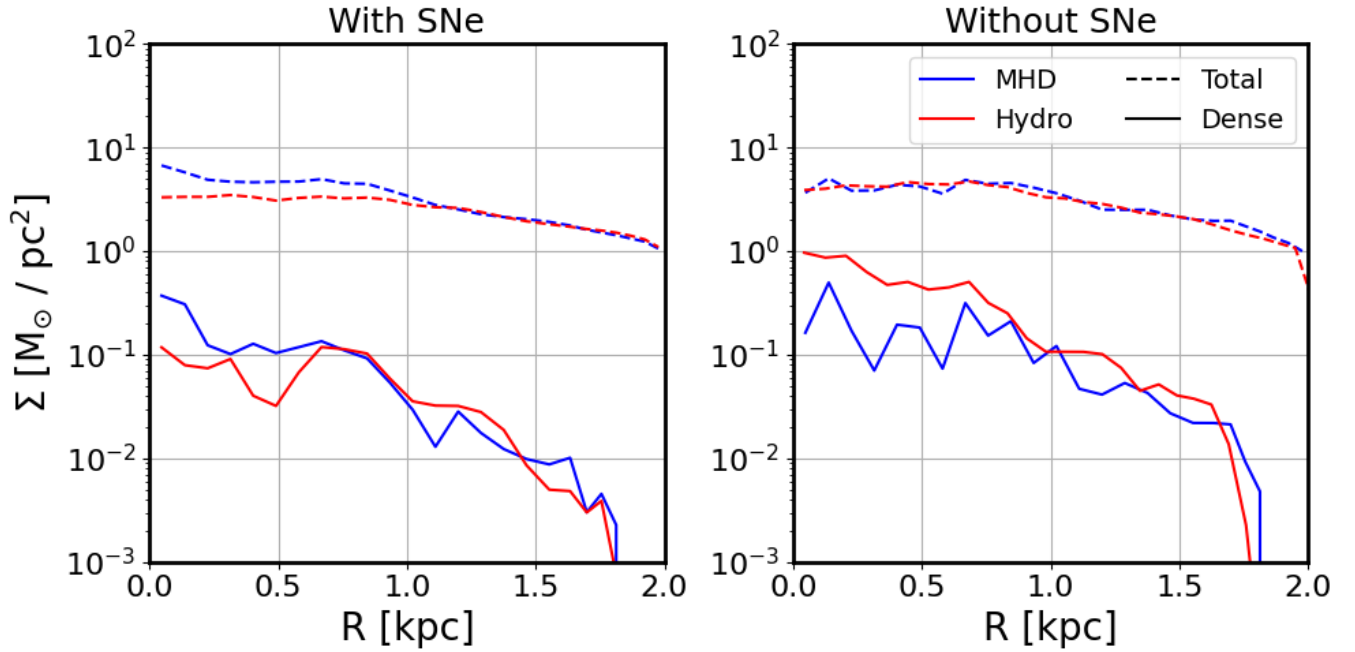


**Figure 4.** The total gas (dashed line) and dense gas (solid line) surface density radial profiles for the MHD (blue) and Hydro (red) simulations with and without SNe averaged over the steady-state period.

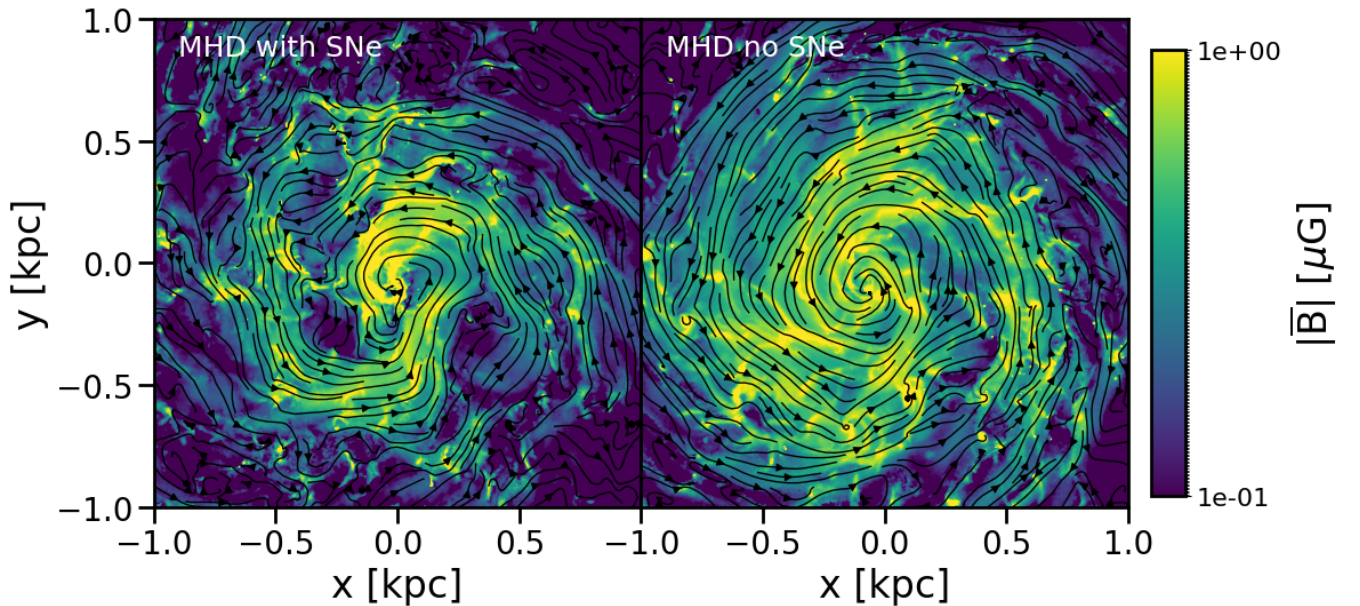


**Figure 5.** The strength of the magnetic field with the field line structure over plotted in the two MHD models presented in this work. The left plot is the model with SNe feedback, the right has no SNe. It is clear in these plots that without feedback the resulting field is more organised and evenly distributed across the disc.

where  $G$  is the gravitational constant,  $\Sigma_g$  is the surface density of the gas and  $\kappa$  is the epicyclic frequency. We assume that  $\sigma$  is the thermal plus turbulent velocity dispersion added in quadrature as:

$$\sigma = \sqrt{\sigma_{\text{therm}}^2 + \sigma_{\text{turb}}^2}, \quad (9)$$

where  $\sigma_{\text{therm}}$  is the sound speed, and  $\sigma_{\text{turb}}$  is the mass-weighted turbulent velocity dispersion of a bin calculated as:

$$\sigma_{\text{turb}} = \sqrt{\frac{\sum_i m_i (v_{\theta,i} - \bar{v}_{\theta})^2}{\sum_i m_i}}, \quad (10)$$

where  $v_{\theta,i}$  is the azimuthal velocity of cell  $i$ ,  $m_i$  is the cell mass, and  $\bar{v}_{\theta}$  is the mass-weighted mean azimuthal velocity in the bin.

In our galactic-scale approximation we compute  $\kappa$  using

Model	SFR ( $M_{\odot}\text{yr}^{-1}$ )	SFR <sub>max</sub> ( $M_{\odot}\text{yr}^{-1}$ )	$t_{\text{ff}}$ (yr)	SFR <sub>max</sub> /SFR	$\epsilon_{\text{ff}}$	$M_{\text{dense}}$ ( $\geq 100\text{cm}^{-3}$ ) ( $M_{\odot}$ )	SFR <sub>specific</sub> ( $\text{yr}^{-1}$ )
Hydro	$1.74 \times 10^{-3}$	0.098	$3.45 \times 10^6$	56.3	0.018	$3.40 \times 10^5$	$5.09 \times 10^{-9}$
Hydro_no_SNe	$12.7 \times 10^{-3}$	0.787	$2.33 \times 10^6$	62.0	0.016	$18.3 \times 10^5$	$7.04 \times 10^{-9}$
MHD	$1.87 \times 10^{-3}$	0.119	$3.58 \times 10^6$	63.6	0.016	$4.35 \times 10^5$	$4.38 \times 10^{-9}$
MHD_no_SNe	$6.17 \times 10^{-3}$	0.314	$2.15 \times 10^6$	50.9	0.020	$6.74 \times 10^5$	$9.15 \times 10^{-9}$

**Table 4.** Computed values for the star formation rate, free fall star formation rate based on the mean (SFR<sub>max</sub>) free fall time of dense gas ( $n \geq 100\text{cm}^{-3}$ ), the average free fall time of dense gas ( $t_{\text{ff}}$ ), the ratio between the SFR<sub>max</sub> and SFR, the efficiency per free-fall time ( $\epsilon_{\text{ff}}$ ), the mean free fall time of dense gas, the average mass of dense gas in each simulation and the final column shows the aver average SFR per unit dense gas mass.

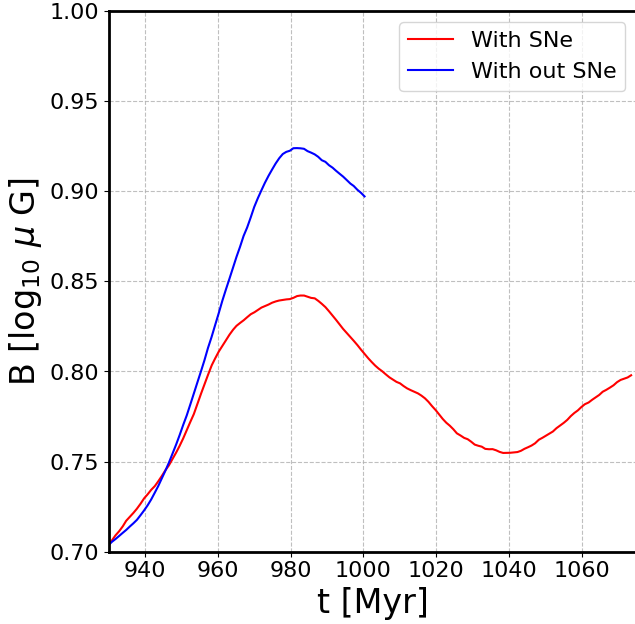


**Figure 6.** volume-weighted magnetic field over time of the two MHD simulations. We see the field grows when feedback is turned off but only by a small amount and appears to be decreasing at the end of the simulation.

the general expression:

$$\kappa^2 = 4\Omega^2 + R \frac{d\Omega^2}{dR}, \quad (11)$$

where  $\Omega$  is  $v_{\text{rot}}/r$  and  $v_{\text{rot}}$  is the mass-weighted mean rotational velocity at each radii. We note that we do not include the stellar component in our calculation, and thus our calculation is only a rough first estimate, considering only the self-gravity of the gas.

The mean and median  $Q$  values for both the total and the dense gas are shown in Table 5, while radial  $Q$  profiles are presented in Figure 12. In all models, the presence of SNe feedback increases  $Q$  and so increases disk stability. Without SNe, the dense gas is significantly more unstable, as seen in the drop in the median  $Q$  from  $\sim 1.09$  (with SNe) to  $\sim 0.50$  (without SNe) in the MHD model, and from  $\sim 1.6$  (with SNe) to  $\sim 0.27$  (without SNe). This can also be clearly seen in Figure 12, where  $Q \sim 1$  in the dense gas in the presence of SNe and magnetic fields up to radii  $\sim 1.5$  kpc and  $Q \lesssim 1$  without SNe. Nevertheless, even in the presence of SNe, the values of  $Q$  for the dense gas still hover around unity which, given our uncertainties, is consistent with marginal instability, and with our observation that the depletion time for the dense

Model		$Q_g$ (Total)	$Q_g$ ( $\geq 100\text{cm}^{-3}$ )
Hydro	Mean	30.24	2.19
	Median	13.63	1.60
Hydro_no_SNe	Mean	11.98	1.13
	Median	9.69	0.267
MHD	Mean	11.88	2.22
	Median	11.24	1.09
MHD_no_SNe	Mean	10.67	0.65
	Median	9.43	0.50

**Table 5.** Mean and median radial Toomre  $Q$  for the total gas and dense gas ( $n \simeq 100\text{cm}^{-3}$ ) within the disc during the steady-state period. We include both the mean and median results here as the mean results could be affected by the large values in the disc centre or at the edges, as can be seen for the large means in both the Hydro  $Q_g$  (Total) and the Hydro\_no\_SNe  $Q_g$  ( $\geq 100\text{cm}^{-3}$ ) and in Figure 12.

gas does not vary significantly between the cases with and without SNe.

## 4 DISCUSSION

There are different ideas on what provides support against collapse of the dense gas and controls star formation, such as, for example, supernova driven turbulence (Padoan et al. 2016) or magnetic fields providing support and reducing the SFR (Hennebelle & Inutsuka 2019; Krumholz & Federrath 2019; Whitworth et al. 2023). In a seminal paper, Zuckerman & Palmer (1974) showed that star formation is inefficient and there have been numerous works (see, e.g., the review by Schinnerer & Leroy 2024, and references therein) that have tried to help explain this. In this work we add to the discussion by looking at dense gas reservoirs and star formation in a galactic context.

### 4.1 Morphology

Focusing on the morphology of the gas in the simulations, Figure 2, we can see the physical effects that SN feedback and magnetic fields have upon the gas distribution. In both models that include feedback we see voids/bubbles and dense filamentary like structures with a distribution of less dense material. The models with magnetic fields appear to have larger and broader filamentary structures. Once the feedback is turned off there is a distinct change in the gas distribution. We begin to see longer filamentary structures appearing to follow the rotation of the disc, forming almost spiral arm-like structures. This is especially noticeable in the Hydro simulation (bottom right plot), where we can see more numerous

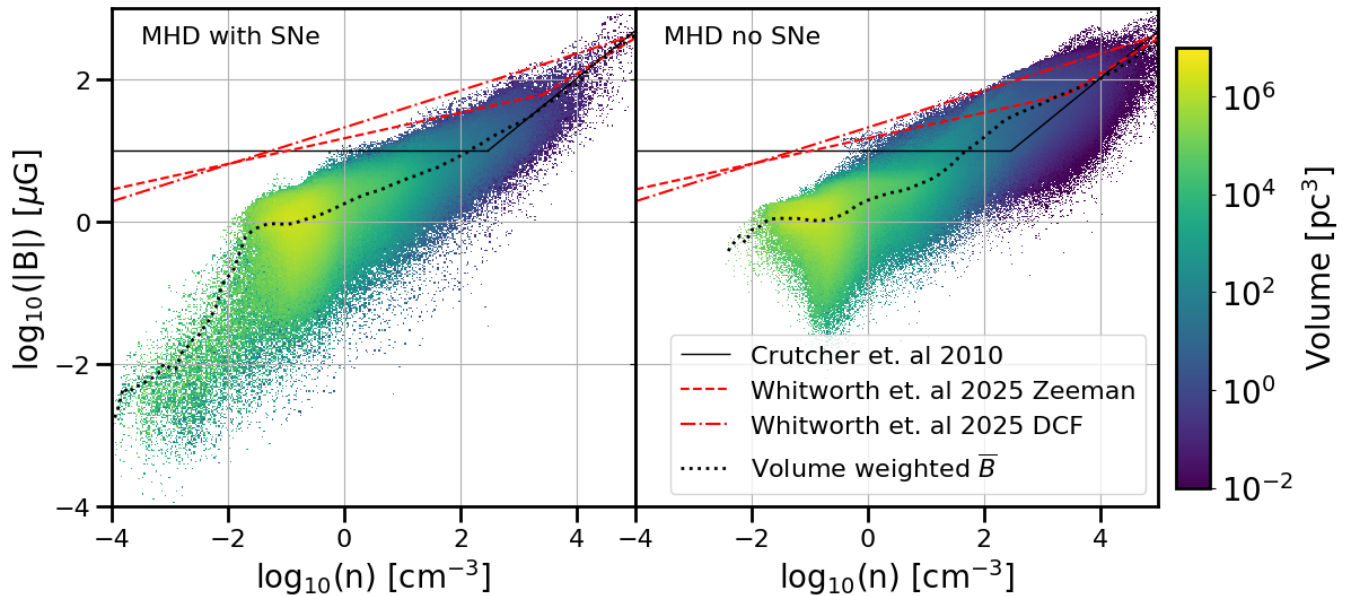


**Figure 7.** The  $B$ - $n$  relationship in the two MHD simulations. The black line represents the [Crutcher et al. \(2010\)](#)  $B$ - $n$  relationship, the red dashed line is the Zeeman result from [Whitworth et al. \(2025\)](#) and the dashed dotted line is their DCF result. The black dotted line is the volume-weighted average field strength.

and larger voids (the low density dark regions) compared to the MHD model. The larger filaments are probably a result of the dense gas not being disrupted by the SNe or a lack of turbulent support as suggested by [Padoan et al. \(2016\)](#), and the lack of heating and stirring of the diffuse gas by the SNe, so that it can freely condense to the cold phase by thermal instability. Figure 4 shows clearly that there is more dense gas in the models without SNe, with both solid lines being consistently higher than the models with SNe. This suggests then that the role of SNe is to retard the transition from diffuse warm gas to cold dense gas by thermal condensation.

#### 4.2 Star formation rates and depletion times

As would be expected, when SN feedback is disabled we see an increase in the star formation rate (Figure 8, solid lines). Indeed, if there is nothing to prevent the gas from gravitationally collapsing, then star formation will increase.

However, while, from columns 2 and 3 of Table 4, we see that both the observed (SFR) and the theoretical maximum (SFR<sub>max</sub>) star formation rates increase when SN feedback is turned off (in both the HD and the MHD cases), the increase is in all cases by factors of only a few to several, nowhere near the factor of two orders of magnitude required to resolve the star formation conundrum. Moreover, this increase is not reflected in the ratio of maximum to observed star formation rates, SFR<sub>max</sub>/SFR (fourth column in Table 4), which increases by only  $\sim 10\%$  in the Hydro models and decreases by  $\sim 20\%$  in the MHD case when SN feedback is turned off. However, the theoretical maximum SFR is *always* higher, by a factor of a few, compared to those observed when SNe or magnetic fields are present.

To further appreciate this, the depletion times for the calculated SFR and SFR<sub>max</sub> are shown in Figure 9 and Table 6. We see much shorter depletion times associated with SFR<sub>max</sub>

Model	$\tau_{\text{total}}$ (yr)	$\tau_{\text{dense}}$ (yr)	$\tau_{\text{SFR}_{\text{max}}}$ (yr)	$\tau_{\text{total}} / \tau_{\text{SFR}_{\text{max}}}$
Hydro	$18.0 \times 10^9$	$2.08 \times 10^8$	$2.97 \times 10^8$	60.6
Hydro_no_SNe	$2.36 \times 10^9$	$1.43 \times 10^8$	$0.39 \times 10^8$	60.9
MHD	$18.8 \times 10^9$	$2.46 \times 10^8$	$2.72 \times 10^8$	69.2
MHD_no_SNe	$5.18 \times 10^9$	$1.11 \times 10^8$	$1.01 \times 10^8$	51.3

**Table 6.** The average depletion times for the total gas in the disc, the dense gas and based on the SFR<sub>max</sub> and dense gas.

compared to the total gas in all four simulations. This is to be expected, since SFR<sub>max</sub> is much larger than the actual SFR. Nevertheless, the ratio of  $\tau_{\text{total}}$  to  $\tau_{\text{SFR}_{\text{max}}}$  (last column of Table 6) is not the same as the corresponding (inverse) ratio between the star formation rates (fifth column in Table 4). This reflects a variation in the total gas masses as well (cf. eq. 7).

This hints at feedback affecting the availability of dense gas for star formation, rather than the rate at which dense gas collapses to form stars. So, whilst it appears as though feedback controls the SFR, it is more likely that it is controlling the formation of dense gas, or gas reservoir needed for star formation. If there is more dense gas, there is more star formation.

#### 4.3 Controlling the formation of dense gas

We can see in Table 4 that the mass of dense gas increases when feedback is turned off. In the Hydro case we see a factor  $\sim 5.4$  increase in mass, and in the MHD case an increase of around a factor of  $\sim 1.5$ . These increases do not match the increase in star formation. However, if we look at the SFR *per unit dense gas mass* (SFR<sub>specific</sub>  $\equiv$  SFR/ $M_g = 1/\tau$ ), we see that, when feedback is removed, there is a factor of  $\sim 2.1$  increase in the MHD case, and an increase of  $\sim 1.38$  in the

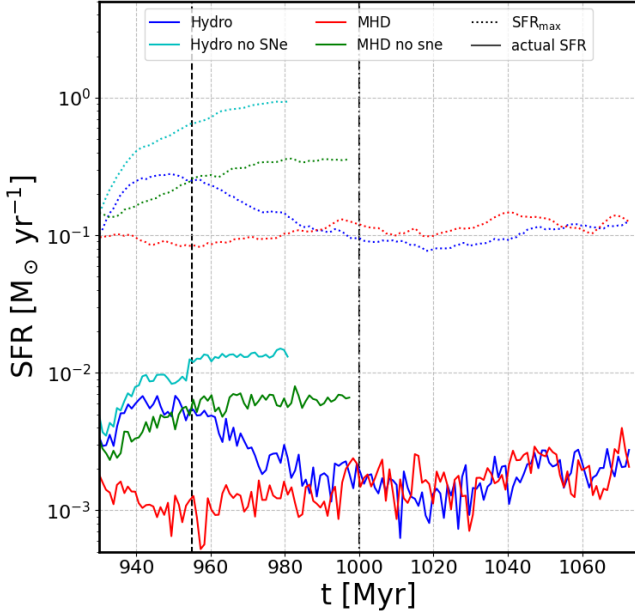


**Figure 8.** The star formation rate (SFR), solid lines, and the maximum free fall star formation rate ( $SFR_{\text{max}}$ ), dotted lines, for each of the models. The black vertical dashed and dash-dotted lines indicate the starting times of the steady-state averaging periods for the Hydro and MHD runs, respectively. The averaging periods extend to the final times of each of the simulations. The starting rates for the new models are slightly higher than the initial model because the rate is based on the difference between the initial snapshot which is the same and the following snapshot where the models begin to diverge. The burst of star formation that occurs in the hydrodynamical model after we turn off the magnetic field can be seen between 930 and 950 Myr. It then settles to a steady state at  $\approx 980$  Myr and is similar to the MHD model. We clearly see that the  $SFR_{\text{max}}$  is nearly 2 orders of magnitude greater than the actual SFR in all cases.

hydro case. So, due to the increase in both mass and SFR, there is only a small increase in  $SFR_{\text{specific}}$ .

From this it appears as though the SN feedback controls the destruction of the dense gas phase rather than the collapse of the dense gas to form stars. With feedback turned on we see less dense gas than when it is absent. If the SN feedback were controlling the conversion of dense gas into stars, and keeping it low, we would expect the SFR per unit dense gas mass to increase to a much greater degree when the SN feedback is turned off. Whilst we do see an increase in SFR, we also see a corresponding increase in dense gas mass. Star formation is therefore controlled by feedback through a regulation of the amount of dense gas and, as this is reduced, the SFR decreases accordingly.

Indeed, Figure 10 shows that once SNe feedback is turned off ( $t = 930$  Myr), the dense gas mass increases with time in both the Hydro and MHD cases (red and blue lines, respectively). This, together with the approximate equality of the depletion times (or, equivalently, of  $SFR_{\text{specific}}$ ) for the cases with and without SNe (the dashed lines in Figure 11 compared to the solid lines), implies that the higher total SFR in the simulations without SNe is essentially driven by an increase in the dense gas mass, not an increase in the collapse rate of the latter. This is also supported by Figure 12, which

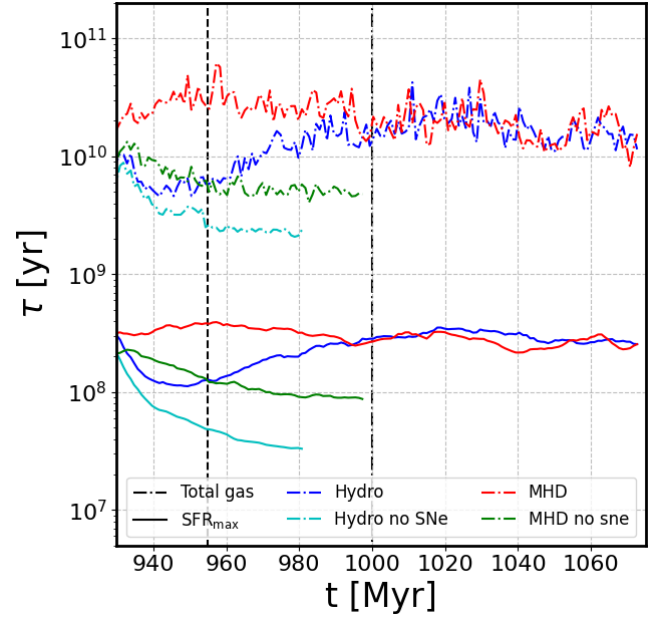


**Figure 9.** The gas depletion time ( $\tau$ ) for the calculated SFR in total gas mass (solid lines), for the free fall star formation rate ( $SFR_{\text{max}}$ ) (dotted lines) and for the calculated SFR in the dense gas (dashed lines). As expected, we lose gas quicker with higher  $SFR_{\text{max}}$ , and therefore will deplete quicker with no SNe feedback.

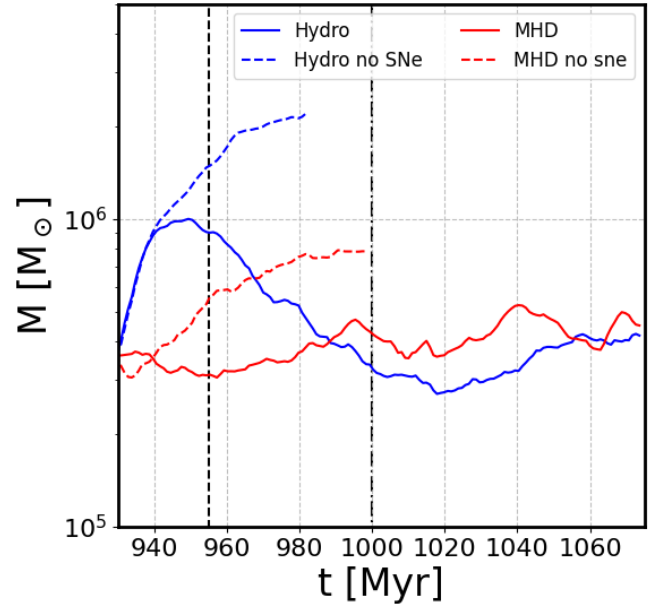


**Figure 10.** The gas mass of different components of the simulations. In the simulations without SNe, the feedback is turned off at the starting time of the plot ( $t = 930$  Myr).

shows the mass-weighted, azimuthally-averaged radial profile of the Toomre  $Q$ , calculated using the turbulent velocity dispersion, for all our simulations. We see that the dense gas is mostly Toomre-unstable for  $R \lesssim 1.5$  kpc, even when SNe are included. We therefore conclude that the main role of the SNe is *not* to prevent the collapse of the dense gas, but to

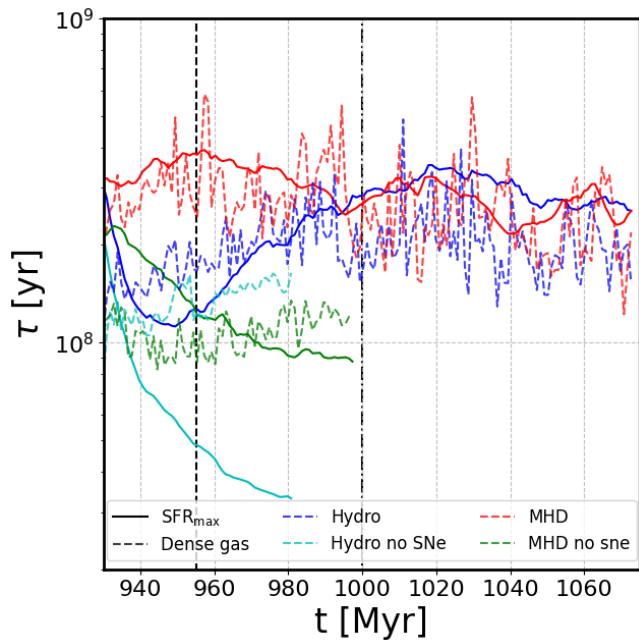


**Figure 11.** The gas depletion time ( $\tau$ ) for the calculated SFR in total gas mass (solid lines), for the free fall star formation rate ( $\text{SFR}_{\text{max}}$ ) (dotted lines) and for the calculated SFR in the dense gas (dashed lines). As expected, we loose gas quicker with higher  $\text{SFR}_{\text{max}}$ , and therefore will deplete quicker with no SNe feedback.

limit its total amount, either by preventing its formation, or by destroying part of the existing dense gas.

Also notable is the fact that the total SFR is always much smaller than the theoretical limit  $\text{SFR}_{\text{max}}$ , even in the absence of SN feedback and magnetic field. In this case, the only form of support remaining is stabilization by rotation, which we suggest is the main supporting mechanism that prevents the collapse at the rate  $\text{SFR}_{\text{max}}$ .

#### 4.4 The efficiency per free fall time

The so-called *efficiency per free-fall time*,

$$\epsilon_{\text{ff}} = \frac{\text{SFR}}{\left(\frac{M_{\text{gas}}}{\tau_{\text{ff}}}\right)}, \quad (12)$$

where  $\tau_{\text{ff}}$  is the free fall time corresponding to the mean density of the dense gas mass  $M_{\text{gas}}$ , was proposed by [Krumholz & McKee \(2005\)](#) as the fraction of the dense gas mass that gets converted into stars over a free-fall time, although [Zamora-Avilés et al. \(2025\)](#) have noted that this quantity is not really an efficiency, since it is not constrained to be less than unity, and is more appropriately interpreted as the ratio of the actual SFR to the theoretical maximum  $\text{SFR}_{\text{max}}$ .

The sixth column in Table 4 shows  $\epsilon_{\text{ff}}$  for our four simulations. We note that it is small in all models, *even those in which* feedback is removed. In these models, we could again appeal to the disc rotation as the mechanism maintaining a low  $\epsilon_{\text{ff}}$ . However, similar results have been obtained for  $\epsilon_{\text{ff}}$  in turbulent box simulations without rotation nor feedback by [Zamora-Avilés et al. \(2025\)](#). The latter authors attributed this result not to any form of support, but rather to the specific form of a continuous gravitationally-driven collapse flow,

in which the gas mass that is being converted to stars at any given time is always a small fraction of the total dense gas mass, provided that this mass is also being replenished by accretion from the diffuse medium. This is, therefore, also a possible reason for our observation of a low  $\epsilon_{\text{ff}}$ .

#### 4.5 The role of the magnetic field on the SFR

It has been suggested that magnetic fields reduce star formation in the ISM ([Krumholz & Federrath 2019](#); [Hennebelle & Inutsuka 2019](#)), though to what extent and in what environments is still debated ([Whitworth et al. 2023](#)). Here, we find that when feedback is turned off, the global averaged field strength grows to a higher strength than with SNe, over a few tens of Myr. This, however, is not enough to counteract the increase in star formation generated by the increase in dense gas (see Section 4.3 for more detail). The gravitational collapse is likely more powerful than the minimal additional pressure support being supplied. We do note that, compared to the Hydro simulation without feedback, the SFR is lower, by roughly half. So, whilst in a more realistic system with feedback there is little to no change in the SFR, we do see a reduction when feedback is removed.

Looking at the  $B$ - $n$  relationship, Fig. 7 compared to [Crutcher et al. \(2010\)](#) and [Whitworth et al. \(2025\)](#), neither simulation aligns. Notably, the loss of the diffuse, low field strength tail in the no feedback simulation highlights the loss of hot, diffuse gas driven by SNe. This is significant because it has been suggested that the hot, diffuse, turbulent gas controls the growth of the magnetic field by the small scale dynamo ([Gent et al. 2021](#); [Whitworth et al. 2025](#)). The lack of these low field strengths could be a result of insufficient resolution in the diffuse gas and thus not properly resolving this regime, (see Section 5.3.4 in [Whitworth et al. \(2025\)](#) for a detailed discussion on this).

Figure 8 shows that, after a brief transient after turning the magnetic field off ( $930 < t < 980$  Myr), the Hydro simulation (solid blue line) adjusts its SFR to essentially the same value as that of the MHD run (solid red line), and remains there for the rest of the integration time. Similarly, in Figure 9 we see that the depletion time for the dense gas is virtually indistinguishable between the MHD and Hydro simulations. This suggests that the dense gas mass is also roughly the same in both cases, as indeed it can be seen in the left panel of Figure 4, which shows that both the Hydro and MHD runs including feedback have essentially the same dense gas radial profile.

These results suggest that the magnetic field has a negligible role in regulating the SFR in the presence of SN feedback. And, since we have already established in Sec. 4.2 that the regulation of the SFR by the SNe is accomplished by regulating the dense gas mass, our results suggest then that, in the presence of SN driving, the magnetic field also has a negligible effect in regulating the dense gas mass.

On the other hand, in the case with no SNe, we do see a larger SFR (by a factor  $\sim 2$ ) for the Hydro simulation (cyan solid line in Figure 8) than that for the corresponding MHD run (green solid line). However, the depletion time for the dense gas does not exhibit a corresponding variation from the Hydro to the MHD case (cyan dashed line and green dashed line, respectively in Figure 9 and in Table 6), and instead the two depletion times are within  $\sim 50\%$  from each other. This

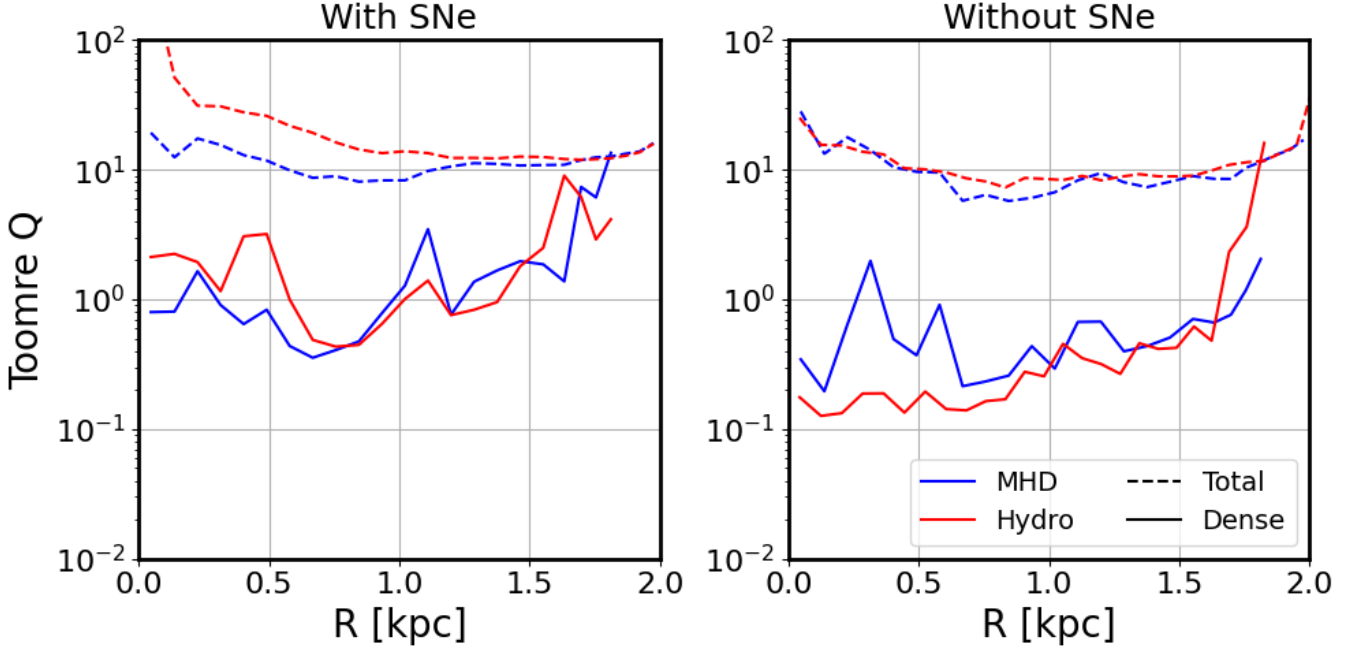


**Figure 12.** The mass-weighted Toomre  $Q$  radial profiles calculated using the thermal and turbulent velocity dispersion averaged over the steady state periods for each model.

is because the Hydro simulation also has a much larger dense gas mass, which nearly compensates for the increased SFR, seen in the right panel of Figure 4.

These results suggest that, in the absence of feedback, the magnetic field does influence the SFR, by preventing the *formation* of dense gas by thermal condensation, presumably by increasing the total pressure of the diffuse gas, rather than by significantly modifying the collapse rate of the dense gas. Indeed, the  $\text{SFR}_{\text{specific}}$  of the dense gas (or, equivalently, its gas depletion time) remains essentially the same with and without the magnetic field, while its mass is nearly 3 times larger in the Hydro case than in the MHD one (always without SNe), as also seen in the 7th column of Table 4.

## 5 CONCLUSIONS

In this paper we have presented four dwarf galaxy simulations with and without magnetic fields and with and without supernova feedback to determine what affects the galactic star formation rates and gas support more. We present our main conclusions here:

- Although the total SFR does increase when SN feedback is turned off, so does the theoretical maximum  $\text{SFR}_{\text{max}}$ , because the dense gas mass also increases. In all cases,  $\text{SFR}_{\text{max}}$  remains nearly 1.75 orders of magnitude larger than the actual measured SFR. This implies that the discrepancy between the actual SFR and  $\text{SFR}_{\text{max}}$  is *not due to SN feedback*.
- When SN feedback is turned off, the SFR per unit mass ( $\text{SFR}_{\text{specific}}$ ) increases by a factor  $\sim 1.38$  in the Hydro case and a factor  $\sim 2.1$  in the MHD case when SNE are removed.
- The depletion time of the dense gas remains within a factor of a few from that of  $\text{SFR}_{\text{max}}$ , indicating that the

dense gas is collapsing at a rate not too different from the free-fall rate.

- The above results indicate that the regulation of the SFR by the SN feedback is accomplished mainly by *regulating the conversion of diffuse to dense gas*, rather than by retarding the collapse of the dense gas.

- The effect of the magnetic field is negligible when SN feedback is on. However, when SNe are off, the presence of the magnetic field acts in a similar way to the feedback, by reducing the total amount of dense gas, suggesting that its main effect is to prevent the conversion of diffuse to dense gas, presumably because the magnetic pressure reduces the thermal condensation of the diffuse gas.

- The discrepancy between the observed and the theoretical maximum SFRs could be attributed in our simulations to the stabilization of the gas provided by the galactic rotation. However, since the same discrepancy has been observed in non-rotating simulations without feedback, and attributed to the specific properties of the collapsing flow in other works, the final stabilization mechanism remains open to further testing.

## ACKNOWLEDGEMENTS

The authors thankfully acknowledge useful comments by Mordecai-Mark Mac Low on the inclusion of the turbulent velocity dispersion in the calculation of the Toomre parameter. D.J.W. acknowledges support from the Programa de Becas Posdoctorales of the Dirección General de Asuntos del Personal Académico of the Universidad Nacional Autónoma de México (DGAPA, UNAM, Mexico) and support from the ANR CASCADE grant (ANR-24-ERCS-0004). E.V.-S. acknowledges financial support from UNAM-PAPIIT grant IG100223. J.B.-P. acknowledges finan-

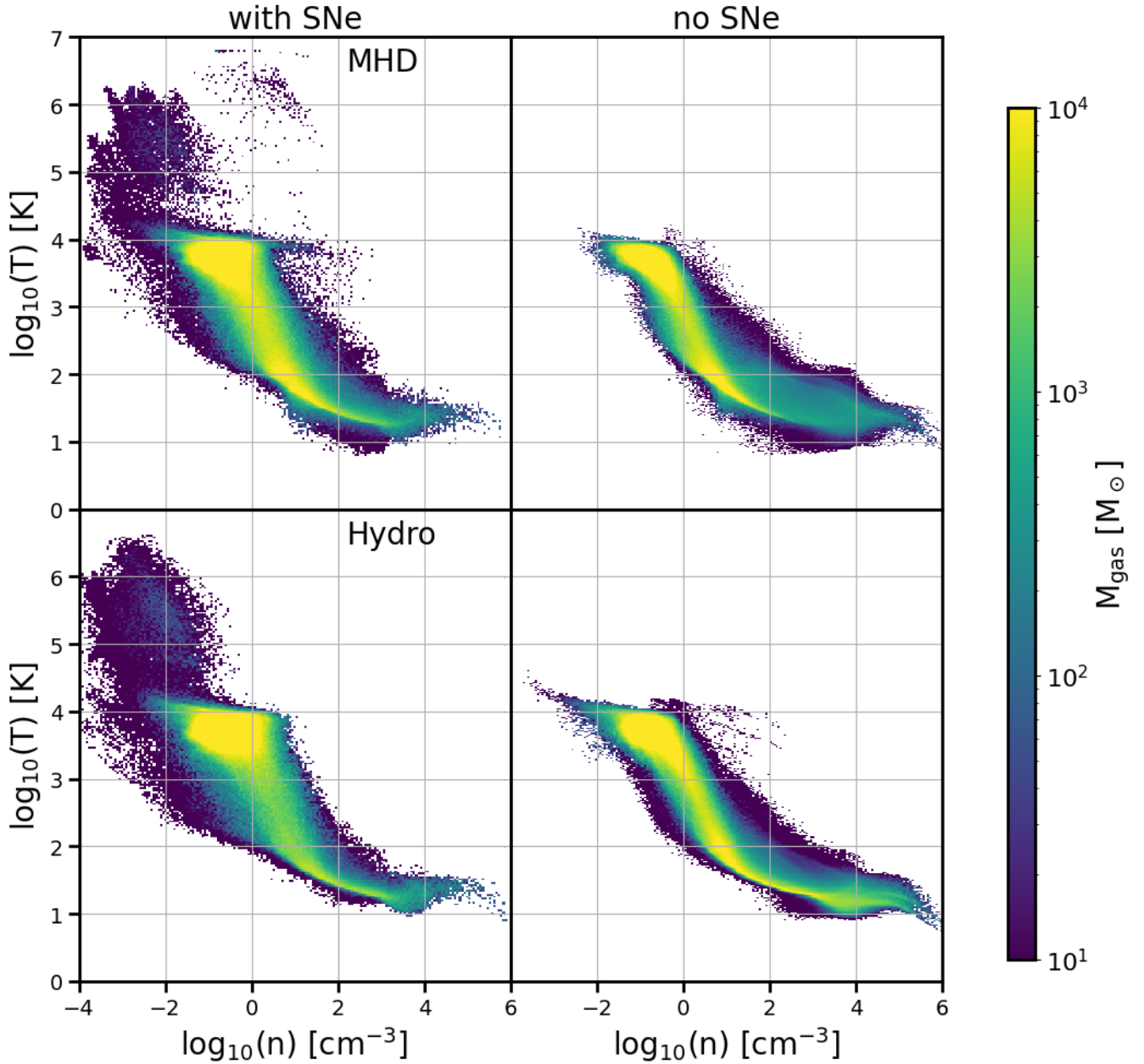


**Figure 13.** Number density phase plots for the gaseous discs of each simulation. We see that in the models with SN feedback the diffuse gas temperature reaches up to  $10^6 \sim 10^7$  K, where as in the models with no SN the temperature reaches maximum of  $\sim 10^4$  K with little to no gas below  $n \sim 0.01 \text{ cm}^{-3}$ . We also see a broadening of the distribution below  $T \sim 100$  K and  $n \sim 1 \text{ cm}^{-3}$ .

cial support from UNAM-PAPIIT grant IN110026. G.C.G. acknowledges support from UNAM-PAPIIT grant IN110824. This work used the DiRAC COSMA Durham facility managed by the Institute for Computational Cosmology on behalf of the STFC DiRAC HPC Facility ([www.dirac.ac.uk](http://www.dirac.ac.uk)). The equipment was funded by BEIS capital funding via STFC capital grants ST/P002293/1, ST/R002371/1 and ST/S002502/1, Durham University and STFC operations grant ST/R000832/1. DiRAC is part of the National e-Infrastructure.

#### DATA AVAILABILITY

All data is available up request to the first author.

#### REFERENCES

- Ballesteros-Paredes J., et al., 2024, *MNRAS*, **534**, 1043  
 Bending T. J. R., Dobbs C. L., Bate M. R., 2022, *MNRAS*, **513**, 2088  
 Bruy N., Hennebelle P., Bournaud F., Colling C., 2020, *ApJ*, **896**, L34  
 Bruy N., Hennebelle P., Colman T., Iteanu S., 2023, *A&A*, **675**, A144

- Chevance M., et al., 2022, *MNRAS*, **509**, 272
- Chomiuk L., Povich M. S., 2011, *AJ*, **142**, 197
- Clark P. C., Glover S. C. O., Klessen R. S., 2012, *MNRAS*, **420**, 745
- Clark P. C., Glover S. C. O., Ragan S. E., Duarte-Cabral A., 2019, *MNRAS*, **486**, 4622
- Colín P., Vázquez-Semadeni E., Gómez G. C., 2013, *MNRAS*, **435**, 1701
- Crutcher R. M., Wandelt B., Heiles C., Falgarone E., Troland T. H., 2010, *ApJ*, **725**, 466
- Evans II N. J., et al., 2009, *ApJS*, **181**, 321
- Evans II N. J., Heyer M., Miville-Deschênes M.-A., Nguyen-Luong Q., Merello M., 2021, *ApJ*, **920**, 126
- Federrath C., Sur S., Schleicher D. R. G., Banerjee R., Klessen R. S., 2011, *ApJ*, **731**, 62
- Field G. B., 1970, *Memoires of the Societe Royale des Sciences de Liege*, **19**, 29
- Franco J., Shore S. N., Tenorio-Tagle G., 1994, *ApJ*, **436**, 795
- Geen S., Hennebelle P., Tremblin P., Rosdahl J., 2016, *MNRAS*, **463**, 3129
- Gent F. A., Mac Low M.-M., Käpylä M. J., Singh N. K., 2021, *ApJ*, **910**, L15
- Glover S. C. O., Federrath C., Mac Low M. M., Klessen R. S., 2010, *MNRAS*, **404**, 2
- Gong M., Ostriker E. C., Wolfire M. G., 2017, *ApJ*, **843**, 38
- Grudić M. Y., Guszejnov D., Offner S. S. R., Rosen A. L., Raju A. N., Faucher-Giguère C.-A., Hopkins P. F., 2022, *MNRAS*, **512**, 216
- Haid S., Walch S., Seifried D., Wunsch R., Dinnbier F., Naab T., 2019, *MNRAS*, **482**, 4062
- Hennebelle P., Inutsuka S.-i., 2019, *Frontiers in Astronomy and Space Sciences*, **6**, 5
- Hernquist L., 1990, *ApJ*, **356**, 359
- Heyer M., Dame T. M., 2015, *ARA&A*, **53**, 583
- Iffrig O., Hennebelle P., 2015, *A&A*, **576**, A95
- Iffrig O., Hennebelle P., 2017, *A&A*, **604**, A70
- Inutsuka S.-i., Inoue T., Iwasaki K., Hosokawa T., 2015, *A&A*, **580**, A49
- Jeans J. H., 1902, *Philosophical Transactions of the Royal Society of London Series A*, **199**, 1
- Khullar S., Matzner C. D., Murray N., Grudić M. Y., Guszejnov D., Wetzel A., Hopkins P. F., 2024, *ApJ*, **973**, 40
- Kim J., et al., 2022, *MNRAS*, **516**, 3006
- Krumholz M. R., Federrath C., 2019, *Frontiers in Astronomy and Space Sciences*, **6**, 7
- Krumholz M. R., McKee C. F., 2005, *ApJ*, **630**, 250
- Krumholz M. R., Lada C. J., Forbrich J., 2025, *The Open Journal of Astrophysics*, **8**, 91
- Mac Low M.-M., Klessen R. S., 2004, *Reviews of Modern Physics*, **76**, 125
- Mac Low M.-M., Burkert A., Ibáñez-Mejía J. C., 2017, *ApJ*, **847**, L10
- Maoz D., Badenes C., 2010, *MNRAS*, **407**, 1314
- Matzner C. D., 2002, *ApJ*, **566**, 302
- McKee C. F., Ostriker E. C., 2007, *ARA&A*, **45**, 565
- Miyoshi T., Kusano K., 2005, *Journal of Computational Physics*, **208**, 315
- Padoan P., Pan L., Haugbølle T., Nordlund Å., 2016, *ApJ*, **822**, 11
- Pakmor R., Bauer A., Springel V., 2011, *MNRAS*, **418**, 1392
- Powell K. G., Roe P. L., Linde T. J., Gombosi T. I., De Zeeuw D. L., 1999, *Journal of Computational Physics*, **154**, 284
- Rafikov R. R., 2001, *MNRAS*, **323**, 445
- Safronov V. S., 1960, *Annales d'Astrophysique*
- Schinnerer E., Leroy A. K., 2024, *ARA&A*, **62**, 369
- Sormani M. C., Treß R. G., Klessen R. S., Glover S. C. O., 2017, *MNRAS*, **466**, 407
- Springel V., 2010, *MNRAS*, **401**, 791
- Toomre A., 1964, *ApJ*, **139**, 1217
- Tress R. G., Smith R. J., Sormani M. C., Glover S. C. O., Klessen R. S., Mac Low M.-M., Clark P. C., 2020, *MNRAS*, **492**, 2973
- Truelove J. K., Klein R. I., McKee C. F., Holliman John H. I., Howell L. H., Greenough J. A., 1997, *ApJ*, **489**, L179
- Vázquez-Semadeni E., Palau A., Ballesteros-Paredes J., Gómez G. C., Zamora-Avilés M., 2019, *MNRAS*, **490**, 3061
- Whitworth D. J., Smith R. J., Tress R., Kay S. T., Glover S. C. O., Sormani M. C., Klessen R. S., 2022, *MNRAS*, **510**, 4146
- Whitworth D. J., Smith R. J., Klessen R. S., Mac Low M.-M., Glover S. C. O., Tress R., Pakmor R., Soler J. D., 2023, *MNRAS*, **520**, 89
- Whitworth D. J., et al., 2025, *MNRAS*,
- Zamora-Avilés M., Vázquez-Semadeni E., Körtgen B., Banerjee R., Hartmann L., 2018, *MNRAS*, **474**, 4824
- Zamora-Avilés M., et al., 2025, *MNRAS*, **541**, 3880
- Zuckerman B., Evans II N. J., 1974, *ApJ*, **192**, L149
- Zuckerman B., Palmer P., 1974, *ARA&A*, **12**, 279

This paper has been typeset from a  $\text{\TeX}/\text{\LaTeX}$  file prepared by the author.